

Hyper-order baryon number fluctuations at finite temperature and density

Wei-jie Fu,² Xiaofeng Luo,¹ Jan M. Pawłowski,^{3,4} Fabian Rennecke,⁵ Rui Wen,² and Shi Yin²

¹*Key Laboratory of Quark & Lepton Physics (MOE) and Institute of Particle Physics,
Central China Normal University, Wuhan 430079, China*

²*School of Physics, Dalian University of Technology, Dalian, 116024, P.R. China*

³*Institut für Theoretische Physik, Universität Heidelberg, Philosophenweg 16, 69120 Heidelberg, Germany*

⁴*ExtreMe Matter Institute EMMI, GSI, Planckstraße 1, D-64291 Darmstadt, Germany*

⁵*Physics Department, Brookhaven National Laboratory, Upton, NY 11973, USA*

We study the fourth- to tenth order (hyper-order) baryon number fluctuations at finite temperature and density in an advanced (QCD-assisted) low energy effective theory that includes low energy quantum, thermal and density fluctuations. At vanishing density our results agree quantitatively, both with lattice QCD simulations for temperatures $T \gtrsim 140$ MeV, and with the hadron resonance gas for $T \lesssim 120$ MeV. Furthermore, we compute the dependence of the baryon number fluctuations on the collision energy, which is compared with recent experimental measurements of the kurtosis and the sixth-order cumulant of the net-proton distribution from the STAR collaboration.

The current approach shows a non-monotonic behavior of higher order cumulants as a function of the beam-energy measured by STAR. In the respective regime the QCD-assisted low energy effective theory used shows no critical behaviour. This asks for a refined analysis of hyper fluctuations within first principles QCD, whose setup is also discussed here.

PACS numbers: 11.30.Rd, 11.10.Wx, 05.10.Cc, 12.38.Mh

I. INTRODUCTION

Lots of effort have been made to study the QCD phase structure at finite temperature and density over the last few decades, both from the experimental and theoretical sides [1–4]. One of the most intriguing open questions concerning the QCD phase diagram is the existence of the critical end point (CEP) [5], which is assumed to be located at the end of the first-order phase transition line in the $T - \mu_B$ phase diagram. Here T and μ_B are referred to the temperature and baryon chemical potential, respectively. In view of the uniqueness and importance of CEP, pinning down its location has played a pivotal role in understanding phases of strongly interacting nuclear matter under extreme conditions. Note that the phase transition at CEP is of genuine second order, and thus the correlation length ξ diverges at this point in the thermodynamic limit. Consequently, critical observables, such as fluctuations of conserved charges that receive contributions in powers of ξ from critical dynamics in the proximity of CEP [6], are employed to explore the location of CEP [1, 7].

By performing beam-energy scans in heavy-ion experiments, the phase diagram can be probed at different chemical potentials. It has been proposed in [6, 8, 9] that non-monotonic variations of conserved charge fluctuations as functions of the beam energy could signal the presence of a CEP. Within the Beam Energy Scan (BES) Program at the Relativistic Heavy Ion Collider (RHIC), significant fluctuation measurements have been performed in Phase I, involving the skewness and kurtosis of the net-proton, net-charge, net-kaon multiplicity distributions [10–13], second-order off-diagonal cumulants, i.e., correlations of net-proton, net-charge, net-kaon multiplicity distributions [14]. Remarkably, very recently the

STAR collaboration has reported the first evidence of a non-monotonic variation in kurtosis \times variance of the net-proton number distribution as a function of the collision energy with 3.0σ significance for central collisions [7]. Moreover, the measurement has also been extended to the sixth-order cumulant of net-proton and net-charge distributions, and preliminary results have been obtained [15, 16].

The study of fluctuations of conserved charges, e.g., the baryon number, electric charge and the strangeness, has always been an active area of theoretical research. Significant progress in this direction has been made within lattice QCD simulations [17–23], in particular in the regime of high T and vanishing μ_B in the phase diagram. It is, however, difficult to extend lattice simulations to the finite- μ_B region due to the sign problem. Remarkably, recent first-principle QCD calculations at finite temperature and density, within both the functional renormalization group (fRG) and Dyson-Schwinger equations (DSE), indicate that the location of CEP is presumably in a region of $450 \text{ MeV} \lesssim \mu_B \lesssim 650 \text{ MeV}$ [3, 4, 24, 25]. Therefore, it is reasonable to expect that the high- μ_B region is quite relevant to the physics of CEP. In fact, there is a wealth of research works concerning the fluctuations and correlations of conserved charges, e.g., within the functional continuum field approaches such as DSE [24, 26] and fRG [27–34], and also in the low energy effective theory [35–39].

In recent years, some of us have investigated skewness and kurtosis of baryon number distributions [30, 31, 40], and baryon-strangeness correlations [33, 34] within QCD-improved low energy effective theories (LEFT) with the fRG. In the present work, we would like to improve on these previous studies, and more importantly focus on hyper-order baryon number fluctuations. Here we use

the terminology “hyper-order” to denote orders higher than the fourth one. In order to obtain a more realistic description of these fluctuations within the LEFT framework, we use input from both QCD and heavy-ion phenomenology. Conventionally, vacuum properties of QCD, such as hadron masses and decay constants, are used to fix the free parameters of the LEFT. However, for the in-medium behavior of baryon number correlations, thermal and density scales are just as important. Here, we use first-principles QCD results on the T -dependence of the kurtosis and the μ_B -dependence of the chiral phase boundary to map the in-medium scales of the LEFT onto QCD. This will improve the reliability of our predictions for the hyper-order fluctuations. Furthermore, phenomenological freeze-out curves will be used to map our results in terms of T and μ_B onto the beam energies of heavy-ion collisions. This allows us to compare our calculations with recent results of lattice simulations in the regime of low μ_B and experimental data in [7, 15, 16], but also to make predictions for hyper-order fluctuations. Implications of the comparison will be discussed in detail.

Using a QCD-improved LEFT approach has various advantages. Most importantly, it is directly embedded in QCD as the relevant low-energy degrees of freedom emerge dynamically from systematically integrating-out the fast partonic modes of QCD [4, 41–44]. In addition, such an approach allows us to capture both critical and non-critical effects in the QCD phase diagram. This is particularly relevant in the present context as the signatures of the CEP mentioned above have been proposed based on the assumption that the system is in the vicinity of the critical point, i.e. in the critical region. Strictly speaking, under such an assumption it can only be shown that the presence of a CEP is a *sufficient* condition to see non-monotonous variations of conserved charge fluctuations. To see whether it is also a *necessary* condition, non-critical effects need to be taken into account. This is indispensable for the accurate interpretation of the experimental results, especially since it is most likely that critical physics can only be observed in a very small region around the CEP, see e.g. [45].

This paper is organized as follows: In Sec. II we give a brief introduction about the fRG flows of QCD and low energy effective theory and their mutual relationship. Thermodynamics and the hyper-order baryon number fluctuations are discussed in Sec. III. In Sec. IV, first of all, we match the scale between QCD and the low energy effective theory, and then, the calculated results are compared with the lattice QCD simulations and experimental measurements. A summary with conclusions is given in Sec. V. Moreover, details of glue potential and flow equations are presented in App. B and App. C, respectively.

$$\partial_t \Gamma_k[\Phi] = \frac{1}{2} \text{ (gluon loop) } - \text{ (ghost loop) } - \text{ (quark loop) } + \frac{1}{2} \text{ (meson loop) }$$

FIG. 1. Diagrammatic representation of the QCD flow equation within the fRG approach. Lines of different types on the r.h.s. of the equation stand for the full propagators of gluon, ghost, quark, and meson, respectively. Note that the mesonic degree of freedom is denoted by double lines with opposite arrows. The crossed circles represent the regulators in the flow equation.

II. QCD AND EMERGENT LOW ENERGY EFFECTIVE THEORIES

At low momentum scales the glue-dynamics of QCD successively decouples due to the QCD mass gap. This decoupling also applied to the dynamical (hadronic) low energy degrees of freedom, finally leaving us with dynamical pions and hence with chiral perturbation theory (χ PT). Indeed, this successive decoupling is at the root of the success of χ PT.

The functional renormalisation group approach to QCD with its successive integrating-out of momentum modes is ideally suited to follow and study this decoupling. Diagrammatically, this is already seen within the flow equation for the QCD effective action, depicted in Fig. 1. The different lines stand for the full non-perturbative propagators of gluon, ghost, quark and for effective hadronic low energy degrees of freedom and the loop momentum q is restricted by the infrared cutoff scale k , $q^2 \lesssim k^2$. The latter emerged within dynamical hadronisation in QCD and do not signal a low energy effective theory, [46–49]. For quantitative QCD applications in the vacuum see [41–44] in the vacuum, for further conceptual developments and the application to the QCD phase structure important for the present work see [4]. The decoupling is now very apparent as the propagators carry the mass gaps m_{gap} of quarks, gluons and quarks and for cutoff scales $k \ll m_{\text{gap}}$ of a given field the respective loop tends towards zero.

More importantly, in this way the emergent low energy effective theory is naturally embedded in QCD, and its ultraviolet parameters (at $\Lambda \lesssim 1 \text{ GeV}$) as well as further input may be directly computed from QCD, leading to *QCD-assisted* low energy effective theories. For more details see in particular [4], and the recent review [50]. Most prominently this embedding has been used for determining the temperature-dependence of the Polyakov loop potential, see [51, 52]. This setup was then applied to the computation of fluctuations in [30, 31, 40] [Wei-jie, please add lit.](#)

In summary this entails, that for sufficiently small momenta k^2 , temperatures T , and also density or quark chemical potential μ_q , the gluon (and ghost) loop in Fig. 1 decouple from the dynamics, and only provide a non-trivial glue background at finite temperature and

chemical potential. The latter is taken into account with the Polyakov loop potential discussed in detail later.

A. Two-flavour setup

For the physics of fluctuations we are interested in $k, T, \mu_B \lesssim 1 \text{ GeV}$. We restrict ourselves to $k \lesssim 700 \text{ MeV}$ and temperatures and quark chemical potentials $T, \mu_q \lesssim 200 \text{ MeV}$. In this regime we are left with the light quarks $q = (u, d)$ and the strange quark s . The latter, while changing the momentum-scale running of the correlation functions, has subleading effects on the form of the fluctuations. Hence, the effect of the momentum-scale running induced by strange fluctuations, will be mimicked here by an appropriate scale matching detailed in Sec. II B. We also the lowest lying hadronic resonances, the pion $\pi = (\pi^\pm, \pi^0)$, and for symmetry reasons, the scalar resonance σ . The other members of the lowest lying multiplet as well as further hadronic resonances produce rather subleading contributions to the offshell dynamics and hence are dropped. The mesonic fields are stored in an $O(4)$ scalar field $\phi = (\sigma, \boldsymbol{\pi})$. Quantum, thermal and density fluctuations with scales $k \lesssim \Lambda = 700 \text{ MeV}$ are taken into account within the fRG, whose dynamics is now reduced to the last two loops in Fig. 1. The respective effective action of QCD in the low energy regime is approximated by

$$\Gamma_k = \int_x \left\{ Z_{q,k} \bar{q} \left[\gamma_\mu \partial_\mu - \gamma_0 (\hat{\mu} + ig A_0) \right] q + \frac{1}{2} Z_{\phi,k} (\partial_\mu \phi)^2 + h_k \bar{q} (\tau^0 \sigma + \boldsymbol{\tau} \cdot \boldsymbol{\pi}) q + V_k(\rho, A_0) - c\sigma \right\}, \quad (1)$$

with $\int_x = \int_0^{1/T} dx_0 \int d^3x$ and $\tau = 1/2(1, i\gamma_5 \boldsymbol{\sigma})$. In (1), $Z_{q,k}$ and $Z_{\phi,k}$ are the wave function renormalisations for the light quarks and the meson respectively. Further running couplings considered are the Yukawa coupling h_k , the scattering between quarks and mesons, as well as the effective potential $V_k(\rho, A_0)$, that describes the multi-scattering of mesons in the non-trivial glue background present at finite temperature and chemical potential.

This potential has contributions $V_{\text{glue},k}(A_0)$ from off-shell glue fluctuations (first two diagrams in Fig. 1), and contributions $V_{\text{mat},k}(\rho, A_0)$ from the quark loop (third diagram in Fig. 1). This leads us to

$$V_k(\rho, A_0) = V_{\text{glue},k}(A_0) + V_{\text{mat},k}(\rho, A_0), \quad (2)$$

The first contribution is typically reformulated in terms of the Polyakov loop $L(A_0)$, while the latter is directly computed from the present low energy flow. This allows us to trade the A_0 -dependence for that of the traced Polyakov loop, $L(A_0), \bar{L}(A_0)$, see Sec. B, (B2), leading us to the final form of our potential,

$$V_k(\rho, L, \bar{L}) = V_k(\rho, A_0). \quad (3)$$

More details about $V_{\text{glue},k}$ used in this work can be found in Sec. B.

B. 2 + 1-favour scale matching in 2-flavour QCD

The current QCD-assisted LEFT setup enables us to compute thermodynamic observables and in particular hyper-order baryon number fluctuations. However, as already briefly discussed in Sec. II A, we have dropped the dynamics of the strange quark. While we expect sub-dominant effects on hyper-fluctuations, the s -quark influences the momentum running of the correlations in the ultraviolet. In [4] it has been observed on the basis of genuine $N_f = 2$ and $N_f = 2 + 1$ flavour computations in QCD, that the latter effect is well approximated by a respective universal scale-matching of the two-flavour results even in QCD. Such a scale-matching already led to a rather quantitative agreement of thermodynamics and kurtosis within the current LEFT setup with lattice results, see [30, 31, 40].

Definition of R_{nm} still missing!!

Here we briefly describe and adapt this scale matching within the current application: a first consequence of the lack of strange dynamics is the necessity to match the pseudocritical temperature of the chiral phase crossover, i.e., the value of T_c at $\mu_B = 0$ (see also the QCD study in [4]). By now this value in $N_f = 2 + 1$ flavour QCD is well-determined with functional approaches, [4, 25, 53], $T_c = 155.0 \pm 2 \text{ MeV}$, and lattice simulations, $T_c = 156.5 \pm 1.5$ (hotQCD collaboration, [54]), and $T_c = 158.0 \pm 0.6 \text{ MeV}$ (WB collaboration, [55], [please check](#)). Functional approaches also offer well-determined $N_f = 2$ flavour results within the same setup. The comparison of momentum scales in the functional $N_f = 2$ and $N_f = 2 + 1$ flavour results in QCD already leads us to an estimate of $T_c(N_f = 2)/T_c(N_f = 2 + 1) \approx 1.2$.

In the present work we use a $N_f = 2$ -flavour LEFT and not two-flavour QCD. Accordingly we expect a compatible, but potentially not fully agreeing scale matching. The scale-matching adapted best to the current application should utilise well-determined observables, that are of interest here and also provide information about the temperature and chemical potential dependence. Therefore we shall the ratio $R_{42}^B = \chi_4^B/\chi_2^B$ of baryon number fluctuations for the matching of the temperature scale, for its definition see also (13). For the matching of the μ_B -scale we use the curvature κ_2 of the phase boundary.

We denote the temperature and the baryon chemical potential in the $N_f = 2$ -flavour LEFT as T_{LEFT} and $\mu_{B\text{LEFT}}$, respectively. Then, for the QCD scale matching we use a simple linear relation between both, the temperature and chemical potential, to wit,

$$T_{\text{LEFT}} = c_T T, \quad \mu_{B\text{LEFT}} = c_\mu \mu_B, \quad (4)$$

where the constant coefficients c_T and c_μ are to be determined. We emphasise that this linear scale matching is sustained by respective QCD computations in [4], where it works well [Plot?](#).

Specifically, the coefficient c_T in Eq. (4) is adjusted as follows: while the temperature-dependence of the ratio $R_{42}^B = \chi_4^B/\chi_2^B$, see (??), is a prediction of the LEFT, its

absolute temperature has to be adjusted. This is done by minimising (the χ^2 of) the difference between the lattice result and the LEFT-prediction in terms of the rescaled absolute temperature scale in (4) **plot** at $\mu_B = 0$. The respective result is shown in the left panel of Fig. 2, and the two curves match quantitatively supporting the predictive power of the LEFT. This leads us to $c_T = 1.247(12)$.

The coefficient c_μ in Eq. (4) is then determined by the curvature coefficient κ of the phase boundary at vanishing μ_B ,

$$\frac{T_c(\mu_B)}{T_c} = 1 - \kappa \left(\frac{\mu_B}{T_c} \right)^2 + \lambda \left(\frac{\mu_B}{T_c} \right)^4 + \dots \quad (5)$$

The next fourth order expansion coefficient λ is dropped in this determination, as it is very small in both functional, [4, 25, 53] as well as lattice computations, [? ?]. Moreover, the results for the phase boundary at finite chemical potential in [3, 4, 25, 53] reveal that the phase boundary is still described well by the leading order expansion with μ_B^2 -terms. We estimate, that this prediction is quantitatively reliable within $\mu_B/T \lesssim 4$, using results from [3, 4, 25, 53, 56]. This covers the regime studied in the present work.

T_c in Eq. (5) is the pseudocritical temperature at $\mu_B = 0$. Note that the curvature is invariant only if the chemical potential and temperature are rescaled with the same value, and thus the curvature κ_{LEFT} in the LEFT would not be modified if one has $c_\mu = c_T$ in Eq. (4). By employing the order parameter of the chiral phase transition, i.e., the expectation value of the sigma field $\langle \sigma \rangle$ in Eq. (1), we obtain $\kappa_{LEFT} = 0.0193$ in the $N_f = 2$ flavor LEFT. For more discussions about the phase boundary and curvature, see, e.g., [4]. This value of κ_{LEFT} is a bit larger than recent $N_f = 2 + 1$ lattice results, e.g., $\kappa = 0.015(4)$ in [54], $\kappa = 0.0149(21)$ in [57], $\kappa = 0.0153(18)$ in [55]. This mismatch of the curvature between the LEFT and lattice QCD, however, is cured through a suitable choice for the ratio c_μ/c_T in Eq. (4), and one readily arrives at

$$c_\mu = c_T \left(\frac{\kappa}{\kappa_{LEFT}} \right)^{1/2}. \quad (6)$$

Substituting $\kappa_{LEFT} = 0.0193$, $\kappa = 0.0153(18)$, and $c_T = 1.247(12)$ into the equation above, one obtains $c_\mu = 1.110(66)$. **The errors on our results in the following reflect the uncertainties on these parameters. [Is this correct or did I miss something?]**

To sum up, in this section the scales between the LEFT and QCD have been matched by resorting to two observables, i.e., R_{42}^B as a function of T at vanishing chemical potential and the curvature of phase boundary κ , which are both quite relevant to predictions of the hyper-order baryon number fluctuations at finite temperature and densities, to be discussed in the following.

III. THERMODYNAMICS AND HYPER-ORDER BARYON NUMBER FLUCTUATIONS

The thermodynamical potential density in the LEFT at finite temperature and nonzero baryon chemical potential is readily obtained from the effective action in (1) or rather from its integrated flow: we evaluate the effective action on the solution of the quantum equations of motion (EoMs). In the present work we consider only homogeneous (constant) solutions, $(\sigma_{\text{EoM}}, A_{0,\text{EoM}})$ with

$$\frac{\partial V(\rho, L, \bar{L})}{\partial \sigma} = \frac{\partial V(\rho, L, \bar{L})}{\partial L} = \frac{\partial V(\rho, L, \bar{L})}{\partial \bar{L}} = 0, \quad (7)$$

while the quark fields vanish, $q, \bar{q} = 0$. We also note that homogeneous have to be taken with a grain of salt for larger chemical potentials with $\mu_B/T \gtrsim 4$, see [4]. With this preparations we are led to the grand potential $\Omega[T, \mu_B] = V_{k=0}(\rho, L, \bar{L})$, that is the effective potential, evaluated at vanishing cutoff scale $k = 0$. It reads

$$\Omega[T, \mu_B] = V_{\text{glue}}(L, \bar{L}) + V_{\text{mat}}(\rho, L, \bar{L}) - c\sigma, \quad (8)$$

where the gluonic background field A_0 in (2) has been reformulated in terms of the Polyakov loop L and its complex conjugate \bar{L} . As mentioned before, the matter sector of the effective potential is integrated out towards the IR limit $k = 0$, for details see App. C, while the glue sector is independent of k , see App. B. The pressure of the system is directly related to the thermodynamical potential, as follows

$$p = -\Omega[T, \mu_B]. \quad (9)$$

The generalized susceptibility of the baryon number χ_n^B is defined through the n -order derivative of the pressure w.r.t. the baryon chemical potential, to wit,

$$\chi_n^B = \frac{\partial^n}{\partial (\mu_B/T)^n} \frac{p}{T^4}. \quad (10)$$

The generalized susceptibilities are related to various cumulants of the baryon number distribution, which can be measured in heavy-ion collision experiments through the cumulants of its proxy, i.e., the net proton distribution, see, e.g. [1] for details. For the lowest four orders, one is led to

$$\chi_1^B = \frac{1}{VT^3} \langle N_B \rangle, \quad \chi_2^B = \frac{1}{VT^3} \langle (\delta N_B)^2 \rangle, \quad (11)$$

$$\chi_3^B = \frac{1}{VT^3} \langle (\delta N_B)^3 \rangle, \quad (12)$$

$$\chi_4^B = \frac{1}{VT^3} \left(\langle (\delta N_B)^4 \rangle - 3 \langle (\delta N_B)^2 \rangle^2 \right), \quad (13)$$

with $\langle \dots \rangle$ denoting the ensemble average and $\delta N_B = N_B - \langle N_B \rangle$. Thus the mean value of the net baryon number of the system is given by $M = VT^3 \chi_1^B$, the variance

$\sigma^2 = VT^3\chi_2^B$, skewness $S = \chi_3^B/(\chi_2^B\sigma)$, and the kurtosis $\kappa = \chi_4^B/(\chi_2^B\sigma^2)$, respectively.

In this work emphasis is, however, put on the baryon number fluctuations of order higher than the fourth, i.e., χ_n^B 's ($n > 4$), which are named hyper-order baryon number fluctuations. As same as the low-order ones, the hyper-order susceptibilities are also connected to their respective cumulants, and their relations, taking the fifth through eighth ones for instance, are given as follows

$$\chi_5^B = \frac{1}{VT^3} \left(\langle (\delta N_B)^5 \rangle - 10 \langle (\delta N_B)^2 \rangle \langle (\delta N_B)^3 \rangle \right), \quad (14)$$

$$\chi_6^B = \frac{1}{VT^3} \left(\langle (\delta N_B)^6 \rangle - 15 \langle (\delta N_B)^4 \rangle \langle (\delta N_B)^2 \rangle - 10 \langle (\delta N_B)^3 \rangle^2 + 30 \langle (\delta N_B)^2 \rangle^3 \right), \quad (15)$$

$$\begin{aligned} \chi_7^B = \frac{1}{VT^3} & \left(\langle (\delta N_B)^7 \rangle - 21 \langle (\delta N_B)^5 \rangle \langle (\delta N_B)^2 \rangle \right. \\ & - 35 \langle (\delta N_B)^4 \rangle \langle (\delta N_B)^3 \rangle \\ & \left. + 210 \langle (\delta N_B)^3 \rangle \langle (\delta N_B)^2 \rangle^2 \right), \end{aligned} \quad (16)$$

$$\begin{aligned} \chi_8^B = \frac{1}{VT^3} & \left(\langle (\delta N_B)^8 \rangle - 28 \langle (\delta N_B)^6 \rangle \langle (\delta N_B)^2 \rangle \right. \\ & - 56 \langle (\delta N_B)^5 \rangle \langle (\delta N_B)^3 \rangle - 35 \langle (\delta N_B)^4 \rangle^2 \\ & + 420 \langle (\delta N_B)^4 \rangle \langle (\delta N_B)^2 \rangle^2 \\ & \left. + 560 \langle (\delta N_B)^3 \rangle^2 \langle (\delta N_B)^2 \rangle - 630 \langle (\delta N_B)^2 \rangle^4 \right). \end{aligned} \quad (17)$$

Different aspects of hyper-order fluctuations have been studied in mean-field approximations in the past, see e.g. [37, 38, 58]. However, due to the decisive role that non-perturbative quantum fluctuations play for these quantities, a treatment beyond mean-field, as in the present work, is necessary for their accurate description.

IV. NUMERICAL RESULTS AND DISCUSSIONS

In this section we present and discuss our numerical results. At vanishing chemical potential the lower orders are compared to results from lattice calculations. We then discuss the implications of our predictions for the hyper-order baryon number fluctuations for decreasing collision energies (increasing chemical potential) for heavy-ion collision experiments.

A. Hyper-order baryon number fluctuations

As we have discussed above, the LEFT has been calibrated by use of the curvature of phase boundary and the kurtosis of baryon number distribution as a function of T with $\mu_B = 0$, via a detailed comparison with recent lattice results. Consequently, one could use the LEFT to make predictions for the dependence of R_{42}^B on the chemical potential, as well as the hyper-order baryon number fluctuations at finite temperature and density. In the middle and right panels of Fig. 2, $R_{62}^B = \chi_6^B/\chi_2^B$ and $R_{82}^B = \chi_8^B/\chi_2^B$ are shown versus the temperature with vanishing μ_B , respectively, and in the same way the LEFT and lattice QCD results are compared. Apparently, one observes that, with the increase of the order of fluctuations, errors of lattice calculation increase dramatically. Specifically, the eighth-order fluctuations R_{82}^B obtained by the two collaborations show a significant quantitative difference, although they are roughly consistent with each other qualitatively. It is found that the predicted hyper-order baryon number fluctuations from the LEFT within the fRG, are in qualitative agreement with both lattice results, and even consistent with the Wuppertal-Budapest result quantitatively within the errors. **We also computed the hyper-order fluctuations within a simple hadron resonance gas model [59] and found them to be essentially equal to one with only a very minor monotonic increase with T for $T \lesssim 140$ MeV. This is in agreement with our findings.** Moreover, we have also computed baryon number fluctuations of orders even up to the tenth in the LEFT, and the relevant result $R_{10,2}^B = \chi_{10}^B/\chi_2^B$ is presented in Fig. 3, where the chemical potential is chosen to be vanishing. Note that no lattice results for the tenth-order fluctuation are available for the moment, and the dependence of $R_{10,2}^B$ on the temperature in Fig. 3 is a pure prediction by the LEFT within the fRG approach, which needs to be confirmed by other calculations, e.g., lattice QCD, in the future.

To proceed, we consider the chemical potential dependence of baryon number fluctuations. Expanding the pressure in Eq. (9) in powers of $\hat{\mu}_B \equiv \mu_B/T$ around $\hat{\mu}_B = 0$, one is led to

$$\frac{p}{T^4} = \frac{p}{T^4} \Big|_{\hat{\mu}_B=0} + \sum_{i=1}^{\infty} \frac{\chi_{2i}^B|_{\hat{\mu}_B=0}}{(2i)!} \hat{\mu}_B^{2i}. \quad (18)$$

Truncating the Taylor expansion above up to order of $\hat{\mu}_B^8$ and employing Eq. (10), we obtain the expanded baryon

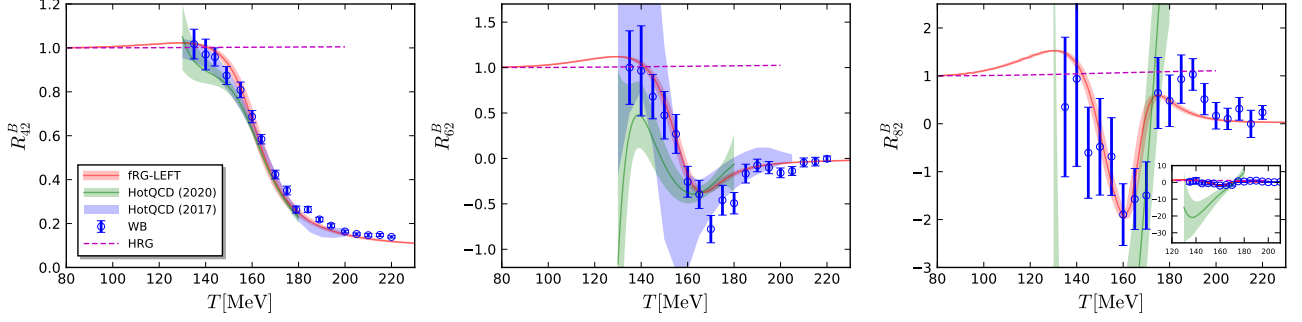


FIG. 2. $R_{42}^B = \chi_4^B / \chi_2^B$ (left panel), $R_{62}^B = \chi_6^B / \chi_2^B$ (middle panel), and $R_{82}^B = \chi_8^B / \chi_2^B$ (right panel) as functions of the temperature with vanishing baryon chemical potential ($\mu_B = 0$). Results obtained with the low energy effective theory within fRG approach are compared with lattice results from the HotQCD collaboration [20, 21, 23] and the Wuppertal-Budapest collaboration [22]. The inset in the plot of R_{82}^B shows its zoom-out view.

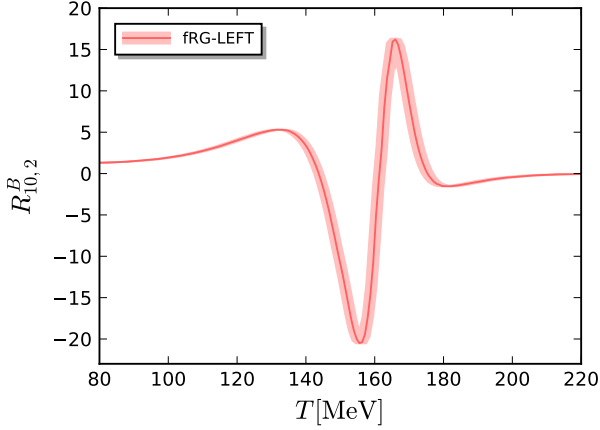


FIG. 3. $R_{10,2}^B = \chi_{10}^B / \chi_2^B$ as a function of the temperature with $\mu_B = 0$, predicted by the LEFT within the fRG approach.

number fluctuations in the first several orders, to wit,

$$\begin{aligned} \chi_2^B &\simeq \chi_2^B|_{\hat{\mu}_B=0} + \frac{\chi_4^B|_{\hat{\mu}_B=0}}{2!} \hat{\mu}_B^2 + \frac{\chi_6^B|_{\hat{\mu}_B=0}}{4!} \hat{\mu}_B^4 \\ &\quad + \frac{\chi_8^B|_{\hat{\mu}_B=0}}{6!} \hat{\mu}_B^6, \end{aligned} \quad (19)$$

$$\chi_4^B \simeq \chi_4^B|_{\hat{\mu}_B=0} + \frac{\chi_6^B|_{\hat{\mu}_B=0}}{2!} \hat{\mu}_B^2 + \frac{\chi_8^B|_{\hat{\mu}_B=0}}{4!} \hat{\mu}_B^4, \quad (20)$$

$$\chi_6^B \simeq \chi_6^B|_{\hat{\mu}_B=0} + \frac{\chi_8^B|_{\hat{\mu}_B=0}}{2!} \hat{\mu}_B^2. \quad (21)$$

In Fig. 4 we show the lattice results χ_4^B / χ_2^B and χ_6^B / χ_2^B based on the Taylor expansion above, and the fluctuations at vanishing chemical potential, viz. $\chi_i^B|_{\hat{\mu}_B=0}$ ($i = 2, 4, 6, 8$) and relevant results in Fig. 2, from the HotQCD collaboration [23] and the Wuppertal-Budapest collaboration [22]. Moreover, χ_n^B 's in Eq. (10) could also be computed directly in the LEFT within the fRG ap-

proach, without resorting to the Taylor expansion, and the relevant results are presented in Fig. 4 for comparison. Here we choose two values of the temperature, and as expected, the LEFT result for the dependence of R_{42}^B and R_{62}^B on the chemical potential, agrees with both lattice results qualitatively, and is even quantitatively consistent with the Wuppertal-Budapest result. Moreover, it is of high interest to investigate the convergence of Taylor expansion in Eqs. (19) (20) (21), via a comparison to the full calculation of baryon number fluctuations in Eq. (10). We have done both calculations in the LEFT-fRG approach, and the relevant results are shown in Fig. 5. One observes that the Taylor expansion in Eqs. (19) (20) (21), where it is expanded up to χ_8^B at vanishing baryon chemical potential for the μ_B -dependence of baryon number fluctuations of lower orders, agrees with the full calculation for R_{42}^B with μ_B/T going up to 1.2, but the convergence upper bound for the higher-order fluctuation R_{62}^B is decreased to ~ 0.8 . We find that the full calculation of R_{62}^B with $\mu_B/T \gtrsim 1.0$ deviates from that of Taylor expansion significantly.

In Fig. 6 R_{42}^B , R_{62}^B and R_{82}^B are depicted as functions of T with several values of μ_B , which are calculated in LEFT with the fRG approach. Relevant results in Fig. 2 for $\mu_B = 0$ are presented as well, in order to highlight effects of the finite baryon chemical potential, whose value is increased from zero to 400 MeV. One observes that both the magnitude and error of the fluctuations, in particular the high-order ones, grow with the increasing chemical potential. Due to the rapid increase of error for very high-order fluctuations at large baryon chemical potential, e.g., R_{82}^B with $\mu_B \gtrsim 200$ MeV, it is reasonable to expect that the LEFT is losing its capability of making predictions in these regimes.

In the following we would like to confront theoretical predictions on the baryon number fluctuations with experimental measurement. Frankly speaking, a direct comparison between the theory and experiment is a challenging task, or even impossible within the setup in this work. This is due to the fact that experimental data are

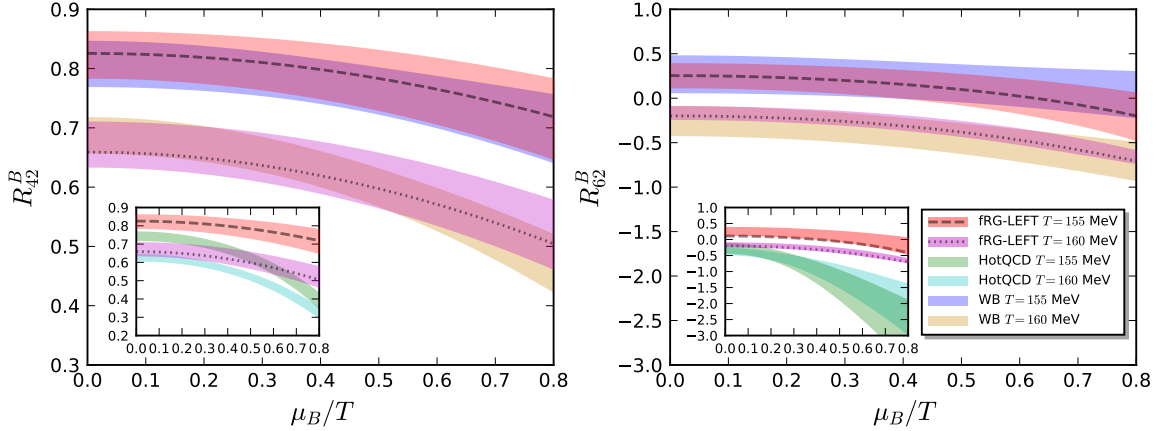


FIG. 4. R_{42}^B (left panel) and R_{62}^B (right panel) as functions of μ_B/T with $T = 155$ MeV and $T = 160$ MeV. Calculation of LEFT within the fRG approach is compared with lattice QCD by the HotQCD collaboration [23] and the Wuppertal-Budapest collaboration [22]. Note that the comparison of R_{42}^B between HotQCD and LEFT is presented in the inlays, in order to improve the readability of presentation.

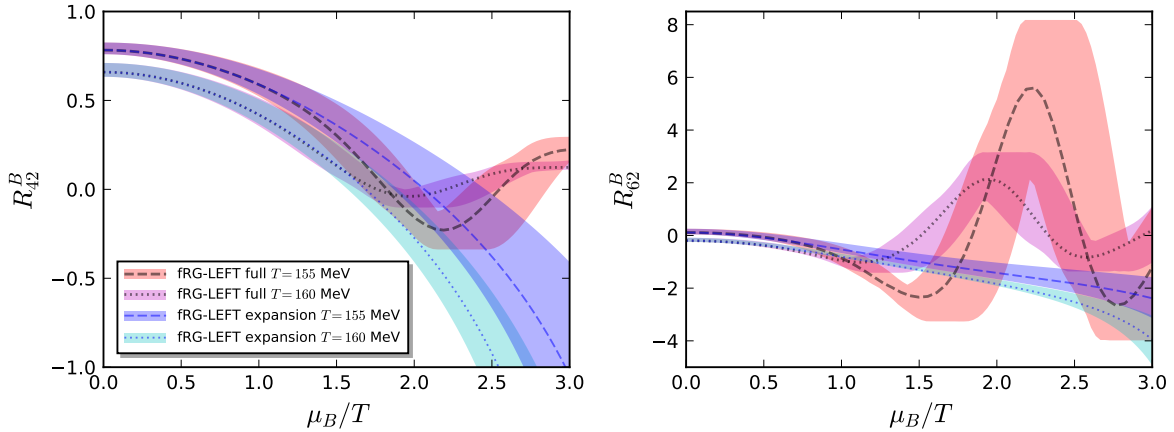


FIG. 5. Comparison between the direct full calculation of baryon number fluctuations R_{42}^B (left panel) and R_{62}^B (right panel) via Eq. (10) and the Taylor expansion in Eqs. (19) (20) (21). Both calculations are performed within the LEFT-fRG approach, and R_{42}^B , R_{62}^B are plotted as functions of μ_B/T with $T = 155$ MeV and $T = 160$ MeV.

affected by many factors, e.g., acceptance of the detector such as the transverse momentum p_T range, rapidity window and the centrality dependence [7, 10, 12, 15, 16], cf. also [1, 61] for more details, volume fluctuations [62], global baryon number conservation [63, 64], resonance decays [65], etc. They constitute the non-critical contributions to fluctuation observables in experiments, and pinning down their contributions plays a pivotal role in identifying the critical signals in the BES experiment. Additionally, **due to critical slowing down, nonequilibrium effects become important in the vicinity of the CEP** [66], which necessitates a theoretical description of the dynamics of critical fluctuations. For more details about recent progress on the dynamics of critical fluctuations in QCD, see [67] and references therein. **We emphasize,**

however, that the present results are well outside the critical region and therefore not subject to critical dynamics.

In this work we will not take into account the non-critical and dynamical effects discussed above when the theoretical results are confronted with experiments, but rather assume that the measured cumulants of the net-proton multiplicity distribution at a given collision energy, with other collision parameters e.g., the centrality and rapidity range fixed, is in one-by-one correspondence to the calculated fluctuations in Eq. (10) with one value of T or μ_B . It is reasonable to attribute the values of T and μ_B to be the ones when the chemical freeze-out occurs, viz. T_{CF} and $\mu_{B,CF}$. Such an approach for the comparison is usually employed in fluctuation studies of equilibrium QCD matter within functional methods or

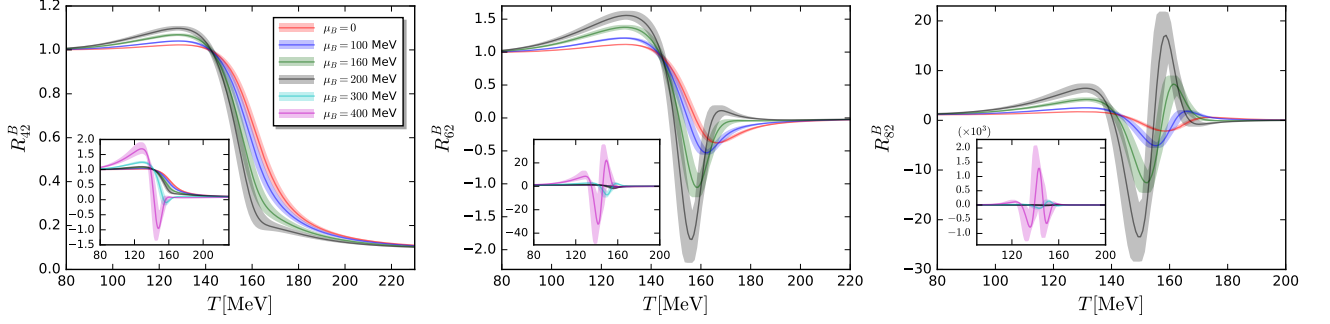


FIG. 6. R_{42}^B (left panel), R_{62}^B (middle panel), and R_{82}^B (right panel) as functions of the temperature at several values of μ_B , computed from LEFT within the fRG approach. Insets in each plot show their respective zoom-out view.

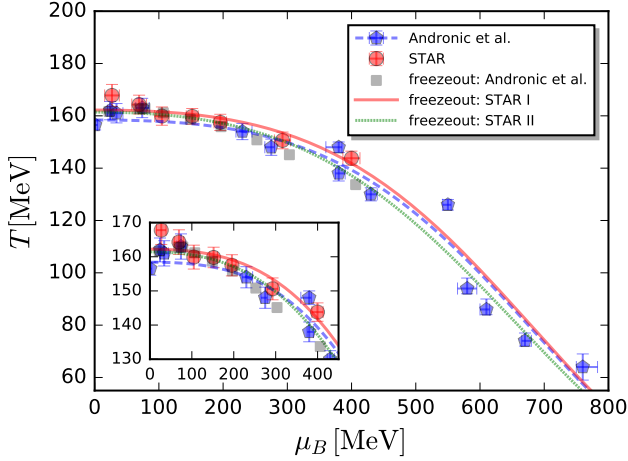


FIG. 7. Chemical freeze-out temperature and baryon chemical potential in the $T - \mu_B$ plane. The blue pentagons and red circles show the freeze-out data from Andronic *et al.* [60] and STAR experiment [61], respectively. The blue dashed line represents the parametrization of blue pentagons through Eqs. (22) and (23). The red solid and green dotted lines show the parametrization of the STAR data based on all the seven data points, and only the four data points in the middle region ($100 \text{ MeV} \lesssim \mu_B \lesssim 300 \text{ MeV}$), respectively. The gray squares are obtained by interpolating the blue pentagons. The inlay zooms in the low- μ_B region.

lattice simulations [23, 24, 31]. Note, however, that because of the reasons we have outlined above, results of comparison between the theory and experiment within this simplified approach should be taken with a grain of salt. In this work we adopt the freeze-out temperature and baryon chemical potential in [60] and in STAR experiment [61], which are shown in Fig. 7 by the blue pentagons and red circles, respectively. They are both obtained from the analysis of hadron yields in the statistical hadron resonance gas model, see aforementioned references for more details. The freeze-out data in [60] has also been parameterized as functions of the collision

energy as follows

$$\mu_{B_{CF}} = \frac{a}{1 + 0.288\sqrt{s_{NN}}}, \quad (22)$$

with $a = 1307.5 \text{ MeV}$, and

$$T_{CF} = \frac{T_{CF}^{lim}}{1 + \exp(2.60 - \ln(\sqrt{s_{NN}})/0.45)}, \quad (23)$$

with $T_{CF}^{lim} = 158.4 \text{ MeV}$. And this parametrization is depicted in Fig. 7 by the blue dashed line. We use the same parametrization functions in Eqs. (22) and (23) to fit the freeze-out data in STAR experiment, i.e., the red circle points in Fig. 7. Two parametrization curves are obtained: the red solid line and the green dotted one, where the former takes all the seven data points into account, while the latter only uses the four data points in the middle region ($100 \text{ MeV} \lesssim \mu_B \lesssim 300 \text{ MeV}$) for the fitting. The freeze-out curves of the red solid and green dotted lines in Fig. 7 are labelled as freezeout: STAR I/II, respectively. The reason why we remove the first two data points in the low μ_B regime and the last one at $\mu_B \sim 400 \text{ MeV}$ in the parametrization of freezeout: STAR II, is due to the fact that the first two points are apparently higher than others and also a general consideration that the freeze-out curve in the plane of $T - \mu_B$ should be convex. One can see that, after these three data points are removed, the freeze-out line of STAR II moves down a bit to lower temperature in comparison to that of STAR I, which is more pronounced when $\mu_B \gtrsim 200 \text{ MeV}$.

In Fig. 8 we show the dependence of baryon number fluctuations R_{42}^B , R_{62}^B , and R_{82}^B on the center-of-mass collision energy, which is calculated in the LEFT within the fRG approach with the freeze-out parameters from Andronic *et al.* [60] and the freeze-out line of STAR I. Note that the freeze-out data from Andronic *et al.* are used through direct interpolation, and the resulting results are shown in Fig. 7 by the gray squares. The theoretical results are also confronted with experimental measurement of cumulants of the net-proton distributions in the beam energy scan experiments from the STAR collaboration. The kurtosis of the net-proton distributions R_{42}^p

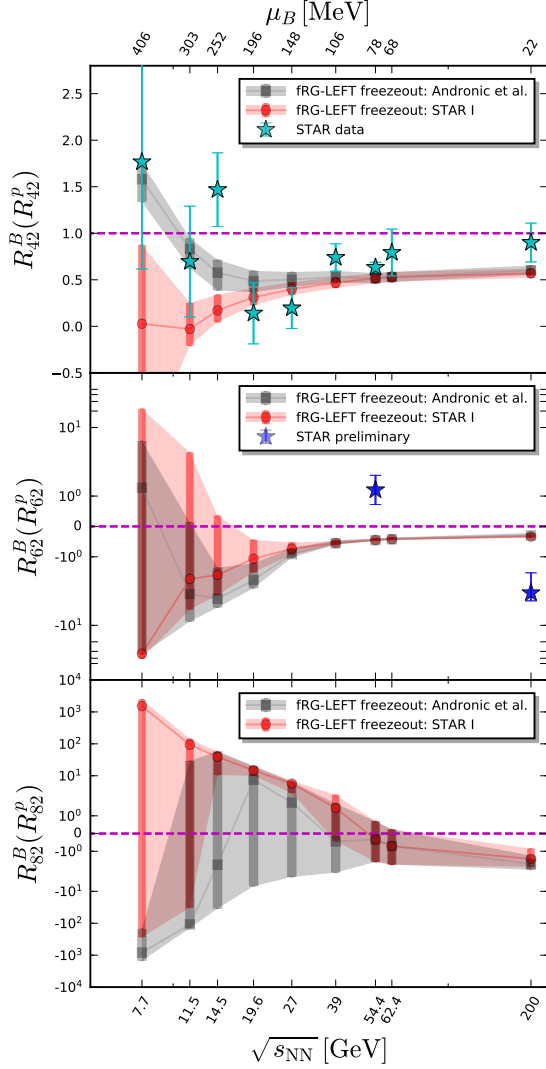


FIG. 8. Baryon number fluctuations R_{42}^B (top), R_{62}^B (middle), and R_{82}^B (bottom) as functions of the collision energy, calculated in LEFT within the fRG approach with the freeze-out parameters from Andronic *et al.* [60] and STAR experiment [61], where the parametrization of STAR freeze-out data is based on all the seven data points as shown in Fig. 7 and is designated as freezeout: STAR I. Experimental data of cumulants from the STAR collaboration are also shown for comparison, where R_{42}^p (top) are the kurtosis of the net-proton distributions measured in Au+Au central (0-5%) collisions [7], and R_{62}^p (middle) is the preliminary result on the six-order cumulant of the net-proton distribution at $\sqrt{s_{NN}}=200$ GeV and 54.4 GeV with centrality 0-40% [15, 16]. The horizontal dashed lines indicate positions of unity for $R_{42}^B(R_{42}^p)$, zeros for $R_{62}^B(R_{62}^p)$ and R_{82}^B .

are measured in Au+Au collisions with centrality 0-5%, transverse momentum range $0.4 < p_T$ (GeV/c) < 2.0 , and rapidity $|y| < 0.5$, cf. [7] for more details. Moreover, preliminary results for the six-order cumulant of the net-proton distribution R_{62}^p are also presented in the middle plot of Fig. 8, which are obtained at two values of the collision energy, i.e., $\sqrt{s_{NN}}=200$ GeV and 54.4 GeV with

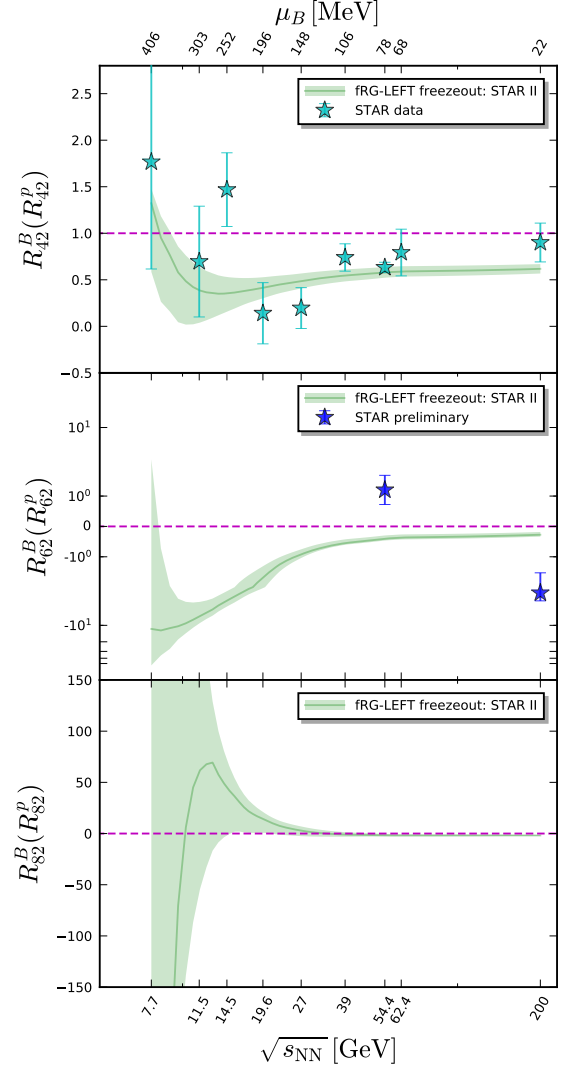


FIG. 9. Baryon number fluctuations R_{42}^B (top), R_{62}^B (middle), and R_{82}^B (bottom) as functions of the collision energy, calculated in LEFT within the fRG approach with the freeze-out parameters from STAR experiment [61], where the parametrization of STAR freeze-out data is based on only the four data points in the middle region ($100 \text{ MeV} \lesssim \mu_B \lesssim 300 \text{ MeV}$) as shown in Fig. 7, and is designated as freezeout: STAR II. Experimental data of cumulants from the STAR collaboration are also shown for comparison, where R_{42}^p (top) are the kurtosis of the net-proton distributions measured in Au+Au central (0-5%) collisions [7], and R_{62}^p (middle) is the preliminary result on the six-order cumulant of the net-proton distribution at $\sqrt{s_{NN}}=200$ GeV and 54.4 GeV with centrality 0-40% [15, 16]. The horizontal dashed lines indicate positions of unity for $R_{42}^B(R_{42}^p)$, zeros for $R_{62}^B(R_{62}^p)$ and R_{82}^B .

centrality 0-40% [15, 16]. In Fig. 9 we show a similar calculation but with the freeze-out line of STAR II, and compare it with the experiment measurement as well.

As shown in Fig. 8 as well as Fig. 9, the theoretical result of the fourth-order fluctuations calculated in the fRG-LEFT approach with the freeze-out data from Andronic *et al.*, as shown by the gray squares and band,

is in qualitative agreement with the experimental measurement of the kurtosis of net-proton distributions. In particular, a nonmonotonic behavior in the low collision energy regime, below ~ 20 GeV, is found in the fRG calculation. The nonmonotonic behavior is also found in the results with the freezeout parametrizations STAR I and STAR II. The nonmonotonic behavior from STAR I is significantly weaker than the others because the freeze-out temperature of STAR I is larger than the two others, in particular in the region of high μ_B , as shown in Fig. 7. This shows that even small variations in the freeze-out temperature have a substantial effect on the fluctuations. The underlying reason is that the freezeout happens in or close to the crossover region, where the fluctuations vary significantly, see Fig. 6.

It is important to emphasize that the strong nonmonotonic behavior of our results for R_{42}^B at small beam-energies in the top panel of Fig. 8 has nothing to do with critical physics. In our model, the CEP is at significantly larger μ_B [do we have a number?], and it is well established that the critical region is only very small, see e.g. [45]. This is a crucial point since a nonmonotonic behavior, e.g., of R_{42}^B as a function of $\sqrt{s_{NN}}$ has been proposed as an experimental signature of a CEP [8, 9]. However, these works only show that critical physics is sufficient for nonmonotonic behavior, it *also* occurs at finite μ_B far away from a CEP. In the present case, it is a result of two effects. First, correlations are enhanced since the chiral crossover becomes sharper with increasing μ_B . This leads to stronger nonmonotonic behavior of R_{42}^B as a function of T (see Fig. 6.). Second, the freeze-out temperature is shifted away from the pseudocritical temperature towards small beam-energies, thereby probing different regimes of the cumulants.

Moreover, the nonmonotonic behavior is also observed in the sixth-order and eighth-order baryon number fluctuations as functions of the collision energy, as shown in the center and bottom panel of Fig. 8 and Fig. 9. The discussion of the previous paragraph clearly also applies here. However, it should be noted that the error of our results increases significantly in the low energy region. These errors include the systematic error of the fRG-LEFT approach, which stem from the uncertainty in the matching of the in-medium scales of the LEFT and QCD, encoded in the coefficients c_T and c_μ in Eq. (4). For $\sqrt{s_{NN}}=200$ GeV and 54.4 GeV we can compare our results for R_{62}^B to preliminary STAR data [15, 16]. As opposed to R_{42}^B , we find large deviations between our and the experimental results. At the highest beam energy, $\sqrt{s_{NN}}=200$ GeV, we at least agree qualitatively in that R_{42}^B is negative.

V. SUMMARY AND CONCLUSIONS

In this work we have studied the baryon number fluctuations in the LEFT within the fRG approach, putting emphasis on the hyper-order ones. The order of baryon number fluctuations has been computed up to the 10th order for the first time beyond mean-field. In our calculations, quantum, thermal and density fluctuations are successively encoded through the evolution of flow equations. Moreover, nontrivial dispersion relation for the quark and meson fields, momentum scale dependence of the quark-meson scattering, and fluctuations of Polyakov loop are also taken into account in this work.

The scale between the LEFT and QCD is matched via a comparison of the temperature dependence of $R_{42}^B = \chi_4^B/\chi_2^B$ at vanishing μ_B between the LEFT and lattice results, as well as a comparison of the curvature of phase boundary. Accordingly, it allows us to employ the LEFT within the fRG approach to make predictions for the μ_B -dependence of R_{42}^B , and the hyper-order baryon number fluctuations at finite temperature and density. In turn, relevant predictions of LEFT are compared with results of lattice QCD simulations. We find that the T - and μ_B -dependence of hyper-order baryon number fluctuations, μ_B -dependence of R_{42}^B obtained in the fRG-LEFT approach, are in quantitative accordance with the lattice results by the Wuppertal-Budapest collaboration within errors. There is still a sizable quantitative deviation in comparison to relevant results by the HotQCD collaboration, but a qualitative consistency is observed.

Furthermore, by employing the commonly used chemical freeze-out temperature and baryon chemical potential from Andronic *et al.* [60] and STAR experiment [61], we obtain baryon number fluctuations R_{42}^B , R_{62}^B , and R_{82}^B as functions of the collision energy, which are compared with experimental measurements of the kurtosis and sixth-order cumulants of the net-proton distributions from the STAR collaboration. Remarkably, the dependence of the fourth-order baryon number fluctuation R_{42}^B on the collision energy obtained in the fRG-LEFT approach, is qualitative consistent with the experimental measured dependence of the kurtosis of net-proton distributions on the collision energy for central collisions. And a nonmonotonic behavior of R_{42}^B as a function of $\sqrt{s_{NN}}$ is found in the fRG calculation. It should, however, be cautioned that errors of R_{42}^B and R_{62}^B increase significantly in the low collision energy region. And when the order of baryon number fluctuations is increased up to the 8th, the theoretical calculation with current setup is losing its capability of making predictions, as a consequence of the significant errors of R_{82}^B for large range of collision energy. Apparently, in order to improve on the computation in this work in the future, and decrease the errors of calculated baryon number fluctuations, especially in the low collision energy regime, on the one hand, the systematic errors of theoretical calculations should be reduced, and on the other hand, chemical freeze-out data with high precision are highly required.

ACKNOWLEDGMENTS

We thank Nu Xu for discussions. The work was supported by the National Natural Science Foundation of China under Contracts Nos. 11775041.

.....

Appendix A: The fRG-approach

A generic quantum field theory is completely described by its effective action $\Gamma[\Phi]$, where Φ is used to denote the collection of all fields in the theory. In the fRG approach, this full quantum effective action is resolved by interpolating it as a function of a renormalization group (RG) scale k , i.e., $\Gamma_k[\Phi]$, successively, starting from the respective classical action $S[\Phi]$ at a very high ultraviolet (UV) scale, say Λ , towards the infrared (IR) limit $k \rightarrow 0$ with $\Gamma[\Phi] = \Gamma_{k=0}[\Phi]$. For more details about the formalism of fRG, see, e.g., [68] as well as [69, 70].

To be specific, the flow equation for QCD, which describes the evolution of its effective action with the RG scale k , is shown in Fig. 1 diagrammatically. As one could see, the QCD flow receives contributions not only from the gluon, ghost and the quark, i.e., the fundamental partonic degrees of freedom in QCD, but also from hadrons, such as mesons, which are composite or emergent degrees of freedom, and are generated dynamically through strong interactions when the RG scale is reduced down to the nonperturbative regime of the low energy QCD. Recent first-principle QCD calculations within fRG indicate that this transition, from the partonic to composite degrees of freedom, takes place in a narrow regime located at $k \sim 1$ GeV [4, 41, 42, 44]. The flow of the QCD effective action corresponding to the diagrams in Fig. 1 can be written as follows,

$$\begin{aligned} \partial_t \Gamma_k[\Phi] = & \frac{1}{2} \text{Tr} \left(G_{AA,k} \partial_t R_{A,k} \right) - \text{Tr} \left(G_{c\bar{c},k} \partial_t R_{c,k} \right) \\ & - \text{Tr} \left(G_{q\bar{q},k} \partial_t R_{q,k} \right) + \frac{1}{2} \text{Tr} \left(G_{\phi\phi,k} \partial_t R_{\phi,k} \right), \end{aligned} \quad (\text{A1})$$

with $\Phi = (A, c, \bar{c}, q, \bar{q}, \phi)$, where G 's and R 's are the propagators and regulators of different fields, respectively. Note that the scale dependence of these quantities is explicitly indicated with a suffix k . The RG time in Eq. (A1) is defined by $t = \ln(k/\Lambda)$, with the initial UV scale Λ . We are not going to discuss details of the QCD flow in Eq. (A1) here, and interested readers are strongly suggested to refer to, e.g., [4, 41, 42, 44, 71–76] for recent progress in understanding of QCD or Yang-Mills theory in the vacuum and at finite temperature and density within the fRG approach, and also [48, 50, 77–82] for QCD related review articles of fRG.

As mentioned above, the transition of the degrees of freedom, from the partonic ones in the perturbative

regime of high energy to the hadronic ones in the non-perturbative region of low energy, is realized through the dynamical hadronization in the fRG approach. With the help of the technique of dynamical hadronization, composite operators of resonated channels, e.g., the σ - π channel, i.e., the scalar-pseudoscalar one in the low energy QCD, which are most relevant to the dynamics of the system, are bosonized or Hubbard-Stratonovich transformed successively with the evolution of RG scale. For more details, see, e.g., [4, 46–49].

In a recent first-principle fRG calculation to QCD, it has been shown clearly that a sequential decoupling of the gluon, quark, and mesonic degrees of freedom from the system with decreasing RG scale, results in a natural emergence of the low energy effective theory (LEFT) when the scale $k \lesssim 1$ GeV [4]. The fRG formalism is ideally suited to the description of a phenomenon of emergence, which usually involves energy scale of different hierarchies, characteristic to different degrees of freedom. When the scale k is high and the system is located in the perturbative region, the only relevant degrees of freedom in QCD are the gluon and quark, and the hadronic or mesonic ones are irrelevant due to their large masses. When k decreases below ~ 1 GeV, the gluon develops a significant mass gap in the low momentum region, and thus decouples from the system. The dynamics is taken over by the emergent composite degrees of freedom, e.g. mesons, in particular the π meson, which is in essence the Goldstone boson related to the spontaneously breaking chiral symmetry in the low energy QCD, and is the lightest hadron of mass ~ 140 MeV in the vacuum.

The matter part of the effective potential $V_{\text{mat},k}$ arises from the quark and meson diagrams in Fig. 1, which is dependent on the meson field through $\rho = \phi^2/2$. Clearly, $V_{\text{mat},k}$ is $\text{SU}_A(2)$ or $\text{O}(4)$ invariant, which guarantees that the chiral symmetry is preserved on the level of interactions. The explicit breaking of the chiral symmetry is attributed to the linear term $-\bar{c}c$ in Eq. (1), which is also related to a nonvanishing value of the current quark mass. The quark chemical potential $\hat{\mu} = \text{diag}(\mu_u, \mu_d)$ in the first line of Eq. (1) is a diagonal matrix in the flavor space, and $\mu = \mu_u = \mu_d$ is assumed throughout this work. The quark chemical potential is related to the baryon chemical potential via $\mu = \mu_B/3$.

In the scale regime of LEFT, as we have discussed above, the flow equation of the effective action in Eq. (A1) is reduced to

$$\partial_t \Gamma_k[\Phi] = - \text{Tr} \left(G_{q\bar{q},k} \partial_t R_{q,k} \right) + \frac{1}{2} \text{Tr} \left(G_{\phi\phi,k} \partial_t R_{\phi,k} \right), \quad (\text{A2})$$

where $R_{q,k}$ and $R_{\phi,k}$ are the regulators for the quark and meson fields, respectively. In this work we employ the $3d$ -flat regulators [83–85], as follows

$$R_{\phi,k}(q_0, \mathbf{q}) = Z_{\phi,k} \mathbf{q}^2 r_B(\mathbf{q}^2/k^2), \quad (\text{A3})$$

$$R_{q,k}(q_0, \mathbf{q}) = Z_{q,k} i \boldsymbol{\gamma} \cdot \mathbf{q} r_F(\mathbf{q}^2/k^2), \quad (\text{A4})$$

with

$$r_B(x) = \left(\frac{1}{x} - 1\right) \Theta(1-x), \quad (\text{A5})$$

$$r_F(x) = \left(\frac{1}{\sqrt{x}} - 1\right) \Theta(1-x), \quad (\text{A6})$$

where $\Theta(x)$ denotes the Heaviside step function. The full propagators read

$$G_{q\bar{q}/\phi\phi,k} = \left(\frac{1}{\Gamma_k^{(2)}[\Phi] + R_k} \right)_{q\bar{q}/\phi\phi}, \quad (\text{A7})$$

with $\Gamma_k^{(2)}[\Phi] = \delta^2 \Gamma_k[\Phi] / (\delta \Phi_{i_1} \delta \Phi_{i_2})$, where different species of fields are distinguished with the help of the subscripts in Φ_{i_1/i_2} . Inserting the effective action (1) into the flow equation (A2), one is led to the flow equation for the effective potential of the matter sector, as follows

$$\begin{aligned} \partial_t V_{\text{mat},k}(\rho) = & \frac{k^4}{4\pi^2} \left[(N_f^2 - 1) l_0^{(B,4)}(\tilde{m}_{\pi,k}^2, \eta_{\phi,k}; T) \right. \\ & + l_0^{(B,4)}(\tilde{m}_{\sigma,k}^2, \eta_{\phi,k}; T) \\ & \left. - 4N_c N_f l_0^{(F,4)}(\tilde{m}_{q,k}^2, \eta_{q,k}; T, \mu) \right], \quad (\text{A8}) \end{aligned}$$

where the threshold functions $l_0^{(B/F,4)}$ as well as other threshold functions in the following can be found in e.g., [4, 86], and the dimensionless renormalized quark and meson masses read

$$\tilde{m}_{q,k}^2 = \frac{h_k^2 \rho}{2k^2 Z_{q,k}^2}, \quad \tilde{m}_{\pi,k}^2 = \frac{V'_{\text{mat},k}(\rho)}{k^2 Z_{\phi,k}}, \quad (\text{A9})$$

$$\tilde{m}_{\sigma,k}^2 = \frac{V'_{\text{mat},k}(\rho) + 2\rho V''_{\text{mat},k}(\rho)}{k^2 Z_{\phi,k}}. \quad (\text{A10})$$

The anomalous dimensions for the quark and meson fields in Eq. (A8) are defined as

$$\eta_{q,k} = -\frac{\partial_t Z_{q,k}}{Z_{q,k}}, \quad \eta_{\phi,k} = -\frac{\partial_t Z_{\phi,k}}{Z_{\phi,k}}, \quad (\text{A11})$$

respectively. Accordingly, projecting the flow in Eq. (A2) onto the one-particle irreducible (1PI) two-point function of the meson, it is readily obtained that

$$\eta_{\phi,k} = -\frac{1}{3Z_{\phi,k}} \delta_{ij} \frac{\partial}{\partial(|\mathbf{p}|^2)} \frac{\delta^2 \partial_t \Gamma_k}{\delta \pi_i(-p) \delta \pi_j(p)} \Big|_{\substack{p_0=0 \\ \mathbf{p}=0}}, \quad (\text{A12})$$

where the spacial component is employed. Note that in the case of finite temperature and density, the $O(4)$ rotation symmetry in the 4- d Euclidean space is broken, and as a matter of fact, the mesonic anomalous dimension extracted above is different from that projected onto

the temporal component. In another word, $\eta_{\phi,k}$ is split into $\eta_{\phi,k}^\perp$ and $\eta_{\phi,k}^\parallel$, which are transverse and longitudinal to the heat bath, respectively, at finite temperature and density. The influences of the splitting of $\eta_{\phi,k}$ on the thermodynamics and baryon number fluctuations have been investigated in detail [86], and it has been found that the impact is small. Therefore, it is reasonable to disregard the splitting of anomalous dimensions, and $\eta_{\phi,k} = \eta_{\phi,k}^\perp = \eta_{\phi,k}^\parallel$, as well as that for the quark anomalous dimension in the following, is assumed throughout this work. In the same way, the quark anomalous dimension is obtained by projecting the relevant flow onto the vector channel of the 1PI quark-antiquark correlation function, as follows

$$\eta_q = \frac{1}{4Z_{q,k}} \times \text{Re} \left[\frac{\partial}{\partial(|\mathbf{p}|^2)} \text{tr} \left(i\boldsymbol{\gamma} \cdot \mathbf{p} \left(-\frac{\delta^2}{\delta \bar{q}(p) \delta q(p)} \partial_t \Gamma_k \right) \right) \right] \Big|_{\substack{p_0,ex \\ \mathbf{p}=0}}, \quad (\text{A13})$$

where the external spacial momentum is chosen to be zero as same as the mesonic one, since the vanishing momentum is most relevant to the flow of effective potential in Eq. (A8). Note that the lowest mode of the fermionic Matsubara frequency is nonvanishing and we designate it here as $p_{0,ex}$, to be described in Appendix C. Moreover, the expression in the square bracket in (A13) is complex-valued, rather than real, when the chemical potential is nonzero. This artifact stems from the naive truncation of the external frequency, which is resolved through a resummation of the external frequency of the quark propagator [40]. The flow equation of the Yukawa coupling is readily obtained via the projection of the 1PI quark-antiquark correlation function on the scalar channel, which reads

$$\partial_t h_k = \frac{1}{2\sigma} \text{Re} \left[\text{tr} \left(-\frac{\delta^2}{\delta \bar{q}(p) \delta q(p)} \partial_t \Gamma_k \right) \right] \Big|_{\substack{p_0,ex \\ \mathbf{p}=0}}. \quad (\text{A14})$$

The explicit expressions for the meson and quark anomalous dimensions, and the flow of the Yukawa coupling can be found in Appendix C.

Appendix B: Glue potential

As we have discussed in Sec. II, the dynamics of the glue sector in QCD is partly imprinted in the glue potential $V_{\text{glue},k}(A_0)$, cf. Eq. (2), when the RG scale is in the regime of LEFT. We neglect the scale dependence of the glue potential in this work, and assume

$$V_{\text{glue}}(L, \bar{L}) = V_{\text{glue},k=0}(A_0) = T^4 \bar{V}_{\text{glue}}(L, \bar{L}), \quad (\text{B1})$$

where we have introduced a dimensionless glue potential \bar{V}_{glue} , and its dependence on the temporal background

A_0 field is realized via the traced Polyakov loop L and its conjugate \bar{L} , which reads

$$L(\mathbf{x}) = \frac{1}{N_c} \langle \text{Tr } \mathcal{P}(\mathbf{x}) \rangle, \quad \bar{L}(\mathbf{x}) = \frac{1}{N_c} \langle \text{Tr } \mathcal{P}^\dagger(\mathbf{x}) \rangle, \quad (\text{B2})$$

with

$$\mathcal{P}(\mathbf{x}) = \mathcal{P} \exp \left(ig \int_0^\beta d\tau \hat{A}_0(\mathbf{x}, \tau) \right), \quad (\text{B3})$$

where \mathcal{P} on the r.h.s. is the path ordering operator. In this work we adopt the parametrization of the glue potential in [87], which reads

$$V_{\text{glue}}(L, \bar{L}) = -\frac{a(T)}{2} \bar{L}L + b(T) \ln M_H(L, \bar{L}) + \frac{c(T)}{2} (L^3 + \bar{L}^3) + d(T) (\bar{L}L)^2, \quad (\text{B4})$$

with the $\text{SU}(N_c)$ Haar measure

$$M_H(L, \bar{L}) = 1 - 6\bar{L}L + 4(L^3 + \bar{L}^3) - 3(\bar{L}L)^2. \quad (\text{B5})$$

Note that the parametrization of glue potential in Eq. (B4), as well as determination of relevant parameters in Tab. I, is done based on lattice results of $\text{SU}(3)$ Yang-Mills theory at finite temperature, where not only the expectation value of the Polyakov loop and pressure, but also quadratic fluctuations of the Polyakov loop are taken into account [87]. The coefficients in Eq. (B4) are dependent on the temperature, which reads

$$x(T) = \frac{x_1 + x_2/(t_r + 1) + x_3/(t_r + 1)^2}{1 + x_4/(t_r + 1) + x_5/(t_r + 1)^2}, \quad (\text{B6})$$

for $x \in \{a, c, d\}$, and

$$b(T) = b_1(t_r + 1)^{-b_4} \left(1 - e^{b_2/(t_r+1)^{b_3}} \right), \quad (\text{B7})$$

with the reduced temperature $t_r = (T - T_c)/T_c$, and the parameters in Eq. (B6) and Eq. (B7) have been fixed in [87] and their values are also collected in Tab. I for convenience.

Though the parametrization of the glue potential in Eq. (B4) is based on results of the Yang-Mills theory, it has found that the unquenching effect in QCD is well captured, once a linear rescaling of the reduced temperature is made from the pure gauge theory to QCD [51, 52, 88], as follows

$$(t_r)_{\text{YM}} \rightarrow \alpha (t_r)_{\text{glue}}, \quad (\text{B8})$$

with

$$(t_r)_{\text{glue}} = (T - T_c^{\text{glue}})/T_c^{\text{glue}}, \quad (\text{B9})$$

where we have used $\alpha = 0.7$ and $T_c^{\text{glue}} = 216$ MeV (in unit of physical temperature via Eq. (4)) in this work.

	1	2	3	4	5
a_i	-44.14	151.4	-90.0677	2.77173	3.56403
b_i	-0.32665	-82.9823	3.0	5.85559	
c_i	-50.7961	114.038	-89.4596	3.08718	6.72812
d_i	27.0885	-56.0859	71.2225	2.9715	6.61433

TABLE I. Values of the parameters in (B6) and (B7) for the glue potential.

Appendix C: Flow equations

The flow equation for the effective potential of the matter sector is given in Eq. (A8). In this work we use the Taylor expansion approach to solve this equation numerically. Expanding the potential around a k -dependent value κ_k , one arrives at

$$V_{\text{mat},k}(\rho) = \sum_{n=0}^{N_v} \frac{\lambda_{n,k}}{n!} (\rho - \kappa_k)^n, \quad (\text{C1})$$

with the expansion coefficients $\lambda_{n,k}$'s, where N_v is the maximal order of Taylor expansion included in the numerical calculation. It is more convenient to rewrite Eq. (C1) by means of the renormalized variables, i.e.,

$$\bar{V}_{\text{mat},k}(\bar{\rho}) = \sum_{n=0}^{N_v} \frac{\bar{\lambda}_{n,k}}{n!} (\bar{\rho} - \bar{\kappa}_k)^n, \quad (\text{C2})$$

with $\bar{V}_{\text{mat},k}(\bar{\rho}) = V_{\text{mat},k}(\rho)$, $\bar{\rho} = Z_{\phi,k}\rho$, $\bar{\kappa}_k = Z_{\phi,k}\kappa_k$, and $\bar{\lambda}_{n,k} = \lambda_{n,k}/(Z_{\phi,k})^n$. Inserting Eq. (C2) into the l.h.s. of Eq. (A8) leads us to

$$\begin{aligned} & \partial_{\bar{\rho}}^n \left(\partial_t \big|_{\bar{\rho}} \bar{V}_{\text{mat},k}(\bar{\rho}) \right) \bigg|_{\bar{\rho}=\bar{\kappa}_k} \\ &= (\partial_t - n\eta_{\phi,k}) \bar{\lambda}_{n,k} - (\partial_t \bar{\kappa}_k + \eta_{\phi,k} \bar{\kappa}_k) \bar{\lambda}_{n+1,k}. \end{aligned} \quad (\text{C3})$$

In our calculation, the expansion point κ_k in Eq. (C1) or $\bar{\kappa}_k$ in Eq. (C2) is chosen such that it is the minimum of the effective action in Eq. (1), which yields the equation of motion as follows

$$\frac{\partial}{\partial \bar{\rho}} \left(\bar{V}_{\text{mat},k}(\bar{\rho}) - \bar{c}_k \bar{\sigma} \right) \bigg|_{\bar{\rho}=\bar{\kappa}_k} = 0, \quad (\text{C4})$$

with $\bar{\sigma} = Z_{\phi,k}^{1/2} \sigma$ and $\bar{c}_k = Z_{\phi,k}^{-1/2} c$, where c is independent of the IR cutoff k . This expansion is usually called the physical running expansion, since the bare expansion point κ_k is k -dependent as mentioned above. In contrast, another commonly used expansion approach is the fixed-point expansion, and as its name suggests, in this approach the bare expansion point is k -independent. For more discussions about these two different expansion approaches, and their advantages and disadvantages in the application of fRG calculations, see

e.g., [30, 42, 86, 89, 90]. Combination of Eq. (C3) and Eq. (C4) leaves us with the flow equation for the expansion point, which reads

$$\begin{aligned} \partial_t \bar{\kappa}_k = & -\frac{\bar{c}_k^2}{\bar{\lambda}_{1,k}^3 + \bar{c}_k^2 \bar{\lambda}_{2,k}} \left[\partial_{\bar{\rho}} \left(\partial_t \big|_{\bar{\rho}} \bar{V}_{\text{mat},k}(\bar{\rho}) \right) \bigg|_{\bar{\rho}=\bar{\kappa}_k} \right. \\ & \left. + \eta_{\phi,k} \left(\frac{\bar{\lambda}_{1,k}}{2} + \bar{\kappa}_k \bar{\lambda}_{2,k} \right) \right]. \end{aligned} \quad (\text{C5})$$

The meson anomalous dimension in Eq. (A12) reads

$$\begin{aligned} \eta_{\phi,k} = & \frac{1}{6\pi^2} \left\{ \frac{4}{k^2} \bar{\kappa}_k (\bar{V}_k''(\bar{\kappa}_k))^2 \mathcal{BB}_{(2,2)}(\tilde{m}_{\pi,k}^2, \tilde{m}_{\sigma,k}^2; T) \right. \\ & + N_c \bar{h}_k^2 \left[\mathcal{F}_{(2)}(\tilde{m}_{q,k}^2; T, \mu) (2\eta_{q,k} - 3) \right. \\ & \left. \left. - 4(\eta_{q,k} - 2) \mathcal{F}_{(3)}(\tilde{m}_{q,k}^2; T, \mu) \right] \right\}, \end{aligned} \quad (\text{C6})$$

The quark anomalous dimension in Eq. (A13) reads

$$\begin{aligned} \eta_{q,k} = & \frac{1}{24\pi^2 N_f} (4 - \eta_{\phi,k}) \bar{h}_k^2 \\ & \times \left\{ (N_f^2 - 1) \mathcal{FB}_{(1,2)}(\tilde{m}_{q,k}^2, \tilde{m}_{\pi,k}^2; T, \mu, p_{0,ex}) \right. \\ & \left. + \mathcal{FB}_{(1,2)}(\tilde{m}_{q,k}^2, \tilde{m}_{\sigma,k}^2; T, \mu, p_{0,ex}) \right\}, \end{aligned} \quad (\text{C7})$$

where in the threshold function \mathcal{FB} 's we have employed $p_{0,ex} = \pi T$ for the finite temperature sector and $p_{0,ex} =$

$\pi T \exp\{-k/(\pi T)\}$ for the vacuum sector. The modification for the vacuum sector is necessitated in order to suppress the artefact of temperature dependence of thermodynamics in the low temperature region [30], which can be resolved by means of frequency summation of the quark external leg [40]. The flow of the Yukawa coupling in Eq. (A14) is given by

$$\begin{aligned} \partial_t \bar{h}_k = & \left(\frac{1}{2} \eta_{\phi,k} + \eta_{q,k} \right) \bar{h}_k(\bar{\rho}) \\ & + \frac{\bar{h}_k^3}{4\pi^2 N_f} \left[L_{(1,1)}^{(4)}(\tilde{m}_{q,k}^2, \tilde{m}_{\sigma,k}^2, \eta_{q,k}, \eta_{\phi,k}; T, \mu, p_{0,ex}) \right. \\ & \left. - (N_f^2 - 1) L_{(1,1)}^{(4)}(\tilde{m}_{q,k}^2, \tilde{m}_{\pi,k}^2, \eta_{q,k}, \eta_{\phi,k}; T, \mu, p_{0,ex}) \right]. \end{aligned} \quad (\text{C8})$$

Note that explicit expressions of all the threshold functions mentioned above, such as \mathcal{BB} , \mathcal{F} 's, \mathcal{FB} 's, and L can be found in e.g., [4, 86].

To summarize, flow equations (A8), (C3), (C5), (C8) supplemented with Eq. (C6) and Eq. (C7) constitute a closed set of ordinary differential equations, which is evolved from the UV cutoff $k = \Lambda$ to the IR limit $k = 0$. The parameters of LEFT are given by initial values of the flow equations. To be specific, the effective potential of the matter sector at the UV cutoff reads

$$V_{\text{mat},k=\Lambda}(\rho) = \frac{\lambda_{k=\Lambda}}{2} \rho^2 + \nu_{k=\Lambda} \rho, \quad (\text{C9})$$

with $\lambda_{k=\Lambda} = 11$ and $\nu_{k=\Lambda} = (0.830 \text{ GeV})^2$. In addition, the initial value of the Yukawa coupling is $h_{k=\Lambda} = 10.18$, and the explicit chiral symmetry breaking parameter is $c = 2.82 \times 10^{-3} \text{ GeV}^3$. These parameters are fixed by fitting the hadronic observables in vacuum, i.e., $f_\pi = 92 \text{ MeV}$, $m_q = 306 \text{ MeV}$, $m_\pi = 136 \text{ MeV}$, and $m_\sigma = 483 \text{ MeV}$.

-
- | | |
|--|--|
| <p>[1] X. Luo and N. Xu, Nucl. Sci. Tech. 28, 112 (2017), arXiv:1701.02105 [nucl-ex].</p> <p>[2] A. Bzdak, S. Esumi, V. Koch, J. Liao, M. Stephanov, and N. Xu, Phys. Rept. 853, 1 (2020), arXiv:1906.00936 [nucl-th].</p> <p>[3] C. S. Fischer, Prog. Part. Nucl. Phys. 105, 1 (2019), arXiv:1810.12938 [hep-ph].</p> <p>[4] W.-j. Fu, J. M. Pawłowski, and F. Rennecke, Phys. Rev. D 101, 054032 (2020), arXiv:1909.02991 [hep-ph].</p> <p>[5] M. A. Stephanov, <i>Proceedings, 24th International Symposium on Lattice Field Theory (Lattice 2006): Tucson, USA, July 23-28, 2006</i>, PoS LAT2006, 024 (2006), arXiv:hep-lat/0701002 [hep-lat].</p> <p>[6] M. Stephanov, Phys. Rev. Lett. 102, 032301 (2009), arXiv:0809.3450 [hep-ph].</p> <p>[7] J. Adam <i>et al.</i> (STAR), (2020), arXiv:2001.02852 [nucl-ex].</p> | <p>[8] M. A. Stephanov, K. Rajagopal, and E. V. Shuryak, Phys. Rev. D60, 114028 (1999), arXiv:hep-ph/9903292 [hep-ph].</p> <p>[9] M. Stephanov, Phys. Rev. Lett. 107, 052301 (2011), arXiv:1104.1627 [hep-ph].</p> <p>[10] L. Adamczyk <i>et al.</i> (STAR), Phys. Rev. Lett. 112, 032302 (2014), arXiv:1309.5681 [nucl-ex].</p> <p>[11] L. Adamczyk <i>et al.</i> (STAR), Phys. Rev. Lett. 113, 092301 (2014), arXiv:1402.1558 [nucl-ex].</p> <p>[12] X. Luo (STAR), <i>Proceedings, 9th International Workshop on Critical Point and Onset of Deconfinement (CPOD 2014): Bielefeld, Germany, November 17-21, 2014</i>, PoS CPOD2014, 019 (2015), arXiv:1503.02558 [nucl-ex].</p> <p>[13] L. Adamczyk <i>et al.</i> (STAR), Phys. Lett. B785, 551 (2018), arXiv:1709.00773 [nucl-ex].</p> <p>[14] J. Adam <i>et al.</i> (STAR), Phys. Rev. C 100, 014902 (2019), arXiv:1903.05370 [nucl-ex].</p> |
|--|--|

- [15] T. Nonaka (STAR), in *28th International Conference on Ultrarelativistic Nucleus-Nucleus Collisions* (2020) arXiv:2002.12505 [nucl-ex].
- [16] A. Pandav (STAR), (2020), arXiv:2003.12503 [nucl-ex].
- [17] A. Bazavov *et al.*, Phys. Rev. Lett. **109**, 192302 (2012), arXiv:1208.1220 [hep-lat].
- [18] S. Borsanyi, Z. Fodor, S. D. Katz, S. Krieg, C. Ratti, and K. K. Szabo, Phys. Rev. Lett. **111**, 062005 (2013), arXiv:1305.5161 [hep-lat].
- [19] S. Borsanyi, Z. Fodor, S. D. Katz, S. Krieg, C. Ratti, and K. K. Szabo, Phys. Rev. Lett. **113**, 052301 (2014), arXiv:1403.4576 [hep-lat].
- [20] A. Bazavov *et al.*, Phys. Rev. **D95**, 054504 (2017), arXiv:1701.04325 [hep-lat].
- [21] A. Bazavov *et al.* (HotQCD), Phys. Rev. **D96**, 074510 (2017), arXiv:1708.04897 [hep-lat].
- [22] S. Borsanyi, Z. Fodor, J. N. Guenther, S. K. Katz, K. K. Szabo, A. Pasztor, I. Portillo, and C. Ratti, JHEP **10**, 205 (2018), arXiv:1805.04445 [hep-lat].
- [23] A. Bazavov *et al.*, Phys. Rev. D **101**, 074502 (2020), arXiv:2001.08530 [hep-lat].
- [24] P. Isserstedt, M. Buballa, C. S. Fischer, and P. J. Gunkel, Phys. Rev. D **100**, 074011 (2019), arXiv:1906.11644 [hep-ph].
- [25] F. Gao and J. M. Pawłowski, (2020), arXiv:2002.07500 [hep-ph].
- [26] X.-y. Xin, S.-x. Qin, and Y.-x. Liu, Phys. Rev. D **90**, 076006 (2014).
- [27] V. Skokov, B. Stokic, B. Friman, and K. Redlich, Phys. Rev. **C82**, 015206 (2010), arXiv:1004.2665 [hep-ph].
- [28] V. Skokov, B. Friman, and K. Redlich, Phys. Rev. **C83**, 054904 (2011), arXiv:1008.4570 [hep-ph].
- [29] K. Morita, B. Friman, and K. Redlich, Phys. Lett. **B741**, 178 (2015), arXiv:1402.5982 [hep-ph].
- [30] W.-j. Fu and J. M. Pawłowski, Phys. Rev. **D92**, 116006 (2015), arXiv:1508.06504 [hep-ph].
- [31] W.-j. Fu and J. M. Pawłowski, Phys. Rev. **D93**, 091501 (2016), arXiv:1512.08461 [hep-ph].
- [32] G. A. Almasi, B. Friman, and K. Redlich, Phys. Rev. D **96**, 014027 (2017), arXiv:1703.05947 [hep-ph].
- [33] W.-j. Fu, J. M. Pawłowski, and F. Rennecke, (2018), 10.21468/SciPostPhysCore.2.1.002, arXiv:1808.00410 [hep-ph].
- [34] W.-j. Fu, J. M. Pawłowski, and F. Rennecke, Phys. Rev. D **100**, 111501 (2019), arXiv:1809.01594 [hep-ph].
- [35] W.-j. Fu, Y.-x. Liu, and Y.-L. Wu, Phys. Rev. D **81**, 014028 (2010), arXiv:0910.5783 [hep-ph].
- [36] W.-j. Fu and Y.-L. Wu, Phys. Rev. D **82**, 074013 (2010), arXiv:1008.3684 [hep-ph].
- [37] F. Karsch, B.-J. Schaefer, M. Wagner, and J. Wambach, Phys. Lett. B **698**, 256 (2011), arXiv:1009.5211 [hep-ph].
- [38] B. Schaefer and M. Wagner, Phys. Rev. D **85**, 034027 (2012), arXiv:1111.6871 [hep-ph].
- [39] Z. Li, K. Xu, X. Wang, and M. Huang, Eur. Phys. J. C **79**, 245 (2019), arXiv:1801.09215 [hep-ph].
- [40] W.-j. Fu, J. M. Pawłowski, F. Rennecke, and B.-J. Schaefer, Phys. Rev. D **94**, 116020 (2016), arXiv:1608.04302 [hep-ph].
- [41] M. Mitter, J. M. Pawłowski, and N. Strodthoff, Phys. Rev. **D91**, 054035 (2015), arXiv:1411.7978 [hep-ph].
- [42] J. Braun, L. Fister, J. M. Pawłowski, and F. Rennecke, Phys. Rev. **D94**, 034016 (2016), arXiv:1412.1045 [hep-ph].
- [43] F. Rennecke, Phys. Rev. **D92**, 076012 (2015), arXiv:1504.03585 [hep-ph].
- [44] A. K. Cyrol, M. Mitter, J. M. Pawłowski, and N. Strodthoff, Phys. Rev. **D97**, 054006 (2018), arXiv:1706.06326 [hep-ph].
- [45] B.-J. Schaefer and J. Wambach, Phys. Rev. **D75**, 085015 (2007), arXiv:hep-ph/0603256 [hep-ph].
- [46] H. Gies and C. Wetterich, Phys. Rev. **D65**, 065001 (2002), arXiv:hep-th/0107221 [hep-th].
- [47] H. Gies and C. Wetterich, Phys. Rev. **D69**, 025001 (2004), arXiv:hep-th/0209183 [hep-th].
- [48] J. M. Pawłowski, Annals Phys. **322**, 2831 (2007), arXiv:hep-th/0512261 [hep-th].
- [49] S. Floerchinger and C. Wetterich, Phys. Lett. **B680**, 371 (2009), arXiv:0905.0915 [hep-th].
- [50] N. Dupuis, L. Canet, A. Eichhorn, W. Metzner, J. Pawłowski, M. Tissier, and N. Wschebor, (2020), arXiv:2006.04853 [cond-mat.stat-mech].
- [51] L. M. Haas, R. Stiele, J. Braun, J. M. Pawłowski, and J. Schaffner-Bielich, Phys. Rev. **D87**, 076004 (2013), arXiv:1302.1993 [hep-ph].
- [52] T. K. Herbst, M. Mitter, J. M. Pawłowski, B.-J. Schaefer, and R. Stiele, Phys. Lett. **B731**, 248 (2014), arXiv:1308.3621 [hep-ph].
- [53] F. Gao and J. M. Pawłowski, (2020), arXiv:2010.13705 [hep-ph].
- [54] A. Bazavov *et al.* (HotQCD), Phys. Lett. **B795**, 15 (2019), arXiv:1812.08235 [hep-lat].
- [55] S. Borsanyi, Z. Fodor, J. N. Guenther, R. Kara, S. D. Katz, P. Parotto, A. Pasztor, C. Ratti, and K. K. Szabo, Phys. Rev. Lett. **125**, 052001 (2020), arXiv:2002.02821 [hep-lat].
- [56] J. Braun, M. Leonhardt, and M. Pospiech, Phys. Rev. **D101**, 036004 (2020), arXiv:1909.06298 [hep-ph].
- [57] R. Bellwied, S. Borsanyi, Z. Fodor, J. Guenther, S. D. Katz, C. Ratti, and K. K. Szabo, Phys. Lett. **B751**, 559 (2015), arXiv:1507.07510 [hep-lat].
- [58] M. Wagner, A. Walther, and B.-J. Schaefer, Comput. Phys. Commun. **181**, 756 (2010), arXiv:0912.2208 [hep-ph].
- [59] P. Braun-Munzinger, K. Redlich, and J. Stachel, , 491 (2003), arXiv:nucl-th/0304013.
- [60] A. Andronic, P. Braun-Munzinger, K. Redlich, and J. Stachel, Nature **561**, 321 (2018), arXiv:1710.09425 [nucl-th].
- [61] L. Adamczyk *et al.* (STAR), Phys. Rev. **C96**, 044904 (2017), arXiv:1701.07065 [nucl-ex].
- [62] X. Luo, J. Xu, B. Mohanty, and N. Xu, J. Phys. G **40**, 105104 (2013), arXiv:1302.2332 [nucl-ex].
- [63] P. Braun-Munzinger, A. Rustamov, and J. Stachel, Nucl. Phys. A **960**, 114 (2017), arXiv:1612.00702 [nucl-th].
- [64] V. Vovchenko, O. Savchuk, R. V. Poberezhnyuk, M. I. Gorenstein, and V. Koch, (2020), arXiv:2003.13905 [hep-ph].
- [65] M. Nahrgang, M. Bluhm, P. Alba, R. Bellwied, and C. Ratti, Eur. Phys. J. C **75**, 573 (2015), arXiv:1402.1238 [hep-ph].
- [66] B. Berdnikov and K. Rajagopal, Phys. Rev. D **61**, 105017 (2000), arXiv:hep-ph/9912274.
- [67] M. Bluhm *et al.*, (2020), arXiv:2001.08831 [nucl-th].
- [68] C. Wetterich, Phys. Lett. **B301**, 90 (1993).
- [69] U. Ellwanger, *Proceedings, Workshop on Quantum field theoretical aspects of high energy physics: Bad Frankenhausen, Germany, September 20-24, 1993*, Z. Phys. **C62**, 503 (1994), [,206(1993)], arXiv:hep-ph/9308260 [hep-ph].

- [70] T. R. Morris, Int. J. Mod. Phys. **A9**, 2411 (1994), arXiv:hep-ph/9308265 [hep-ph].
- [71] J. Braun, H. Gies, and J. M. Pawłowski, Phys.Lett. **B684**, 262 (2010), arXiv:0708.2413 [hep-th].
- [72] J. Braun, Eur. Phys. J. **C64**, 459 (2009), arXiv:0810.1727 [hep-ph].
- [73] J. Braun, L. M. Haas, F. Marhauser, and J. M. Pawłowski, Phys. Rev. Lett. **106**, 022002 (2011), arXiv:0908.0008 [hep-ph].
- [74] A. K. Cyrol, L. Fister, M. Mitter, J. M. Pawłowski, and N. Strodthoff, Phys. Rev. **D94**, 054005 (2016), arXiv:1605.01856 [hep-ph].
- [75] A. K. Cyrol, M. Mitter, J. M. Pawłowski, and N. Strodthoff, Phys. Rev. **D97**, 054015 (2018), arXiv:1708.03482 [hep-ph].
- [76] J. Braun, W.-j. Fu, J. M. Pawłowski, F. Rennecke, D. Rosenblüh, and S. Yin, (2020), arXiv:2003.13112 [hep-ph].
- [77] J. Berges, N. Tetradis, and C. Wetterich, Phys. Rept. **363**, 223 (2002), arXiv:hep-ph/0005122 [hep-ph].
- [78] B.-J. Schaefer and J. Wambach, *Helmholtz International Summer School on Dense Matter in Heavy Ion Collisions and Astrophysics Dubna, Russia, August 21-September 1, 2006*, Phys. Part. Nucl. **39**, 1025 (2008), arXiv:hep-ph/0611191 [hep-ph].
- [79] H. Gies, *Renormalization group and effective field theory approaches to many-body systems*, Lect. Notes Phys. **852**, 287 (2012), arXiv:hep-ph/0611146 [hep-ph].
- [80] O. J. Rosten, Phys. Rept. **511**, 177 (2012), arXiv:1003.1366 [hep-th].
- [81] J. Braun, J. Phys. **G39**, 033001 (2012), arXiv:1108.4449 [hep-ph].
- [82] J. M. Pawłowski, *Proceedings, 24th International Conference on Ultra-Relativistic Nucleus-Nucleus Collisions (Quark Matter 2014): Darmstadt, Germany, May 19-24, 2014*, Nucl. Phys. **A931**, 113 (2014).
- [83] D. F. Litim, Phys. Lett. **B486**, 92 (2000), arXiv:hep-th/0005245 [hep-th].
- [84] D. F. Litim, Phys. Rev. **D64**, 105007 (2001), arXiv:hep-th/0103195 [hep-th].
- [85] D. F. Litim and J. M. Pawłowski, JHEP **11**, 026 (2006), arXiv:hep-th/0609122.
- [86] S. Yin, R. Wen, and W.-j. Fu, Phys. Rev. D **100**, 094029 (2019), arXiv:1907.10262 [hep-ph].
- [87] P. M. Lo, B. Friman, O. Kaczmarek, K. Redlich, and C. Sasaki, Phys. Rev. **D88**, 074502 (2013), arXiv:1307.5958 [hep-lat].
- [88] J. M. Pawłowski, *Proceedings, 9th Conference on Quark Confinement and the Hadron Spectrum: Madrid, Spain, 30 Aug-3 Sep 2010*, AIP Conf. Proc. **1343**, 75 (2011), arXiv:1012.5075 [hep-ph].
- [89] J. M. Pawłowski and F. Rennecke, Phys. Rev. **D90**, 076002 (2014), arXiv:1403.1179 [hep-ph].
- [90] F. Rennecke and B.-J. Schaefer, Phys. Rev. **D96**, 016009 (2017), arXiv:1610.08748 [hep-ph].